Symmetry demanded topological nodal-line materials

Shuo-Ying Yang, Hao Yang, Elena Derunova, Stuart S. P. Parkin, Binghai Yan & Mazhar N. Ali

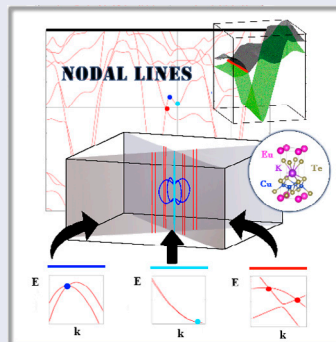Taylor & Francis
Taylor & Francis Group

REVIEW ARTICLE

Symmetry demanded topological nodal-line materials

Shuo-Ying Yang[a], Hao Yang[a,b], Elena Derunova[a], Stuart S. P. Parkin[a], Binghai Yan[b,c] and Mazhar N. Ali[a]

[a]Max Planck Institute of Microstructure Physics, Halle, Germany; [b]Max Planck Institute for Chemical Physics of Solids, Dresden, Germany; [c]Department of Condensed Matter Physics, Weizmann Institute of Science, Rehovot, Israel

ABSTRACT

The realization of Dirac and Weyl physics in solids has made topological materials one of the main focuses of condensed matter physics. Recently, the topic of topological nodal line semimetals, materials in which Dirac or Weyl-like crossings along special lines in momentum space create either a closed ring or line of degeneracies, rather than discrete points, has become a hot topic in topological quantum matter. Here, we review the experimentally confirmed and theoretically predicted topological nodal line semimetals, focusing in particular on the symmetry protection mechanisms of the nodal lines in various materials. Three different mechanisms: a combination of inversion and time-reversal symmetry, mirror reflection symmetry, and non-symmorphic symmetry and their robustness under the effect of spin orbit coupling are discussed. We also present a new Weyl nodal line material, the Te-square net compound KCu_2EuTe_4, which has several Weyl nodal lines including one extremely close to the Fermi level (<30 meV below E_F). Finally, we discuss potential experimental signatures for observing exotic properties of nodal line physics.

CONTACT   Mazhar N. Ali   ✉ maz@berkeley.edu

1. Introduction

Topologically non-trivial states of matter have been of great interest in the field of topological quantum materials during the past decade for their rich and novel physics. The field was ignited after the discovery of topological insulators (TIs) – materials that exhibit robust metallic surface states protected by the topology in the insulating bulk [1,2]. Recently, topological semimetals (TSM) such as Dirac and Weyl semimetals were discovered which can also host metallic surface states with a semi-metallic bulk [3].

Three types of TSMs, Dirac (DSM), Weyl (WSM), and nodal-line semimetals (NLS) have been discovered. A DSM, shown in Figure 1(a), is the result of two doubly degenerate bands crossing near the Fermi level (E_F) at a discrete point in k-space, known as a Dirac point. Demanded by both inversion and time-reversal symmetry, the fourfold degenerate Dirac point has a band dispersion that is linearly dependent with k. Such a linearly dispersed band structure causes the low-energy excitations near the crossing point to be Dirac fermions. The existence of a 3D DSM was first confirmed by angular-resolved photoemission spectroscopy (ARPES) in Na_3Bi [4,5] and Cd_3As_2 [6–8], where the Dirac points are topologically protected by C_3 and C_4 rotation symmetry, respectively [4,9,10]. These materials exhibit many exotic transport properties, such as ultra-high mobility and titanic MR (MR) [9,11–14].

When either inversion symmetry or time-reversal symmetry is broken, doubly degenerate bands become spin split when considering SOC, separating into two singly degenerate band crossings called Weyl points, as shown in Figure 1(b). According to the 'no-go theorem' [15,16], they can only appear in pairs of opposite chirality [17–20]. The existence of Weyl points near the E_F leads to several special characteristics, including Fermi arcs on the surface [18,19,21,22] and the chiral anomaly in the bulk [23–32], among many others [33,34]. The Weyl points can be seen as singularity points of Berry curvature (source or sink), or 'magnetic monopoles' in k-space. The Fermi arcs, unlike closed Fermi surfaces in $2d$ or $3d$ metals, are open 'arcs' that connect the two opposite Weyl points on the boundary. Weyl-like states have first been observed in inversion symmetry-breaking compounds TaAs [35–37], NbAs [38], TaP, NbP [39,40] as well as in photonic crystals [41]. They have also been observed in other inversion symmetry-breaking materials such as $MoTe_2$, WTe_2, and other Ta or Nb monopnictides [21,42–47]. These Weyl particles are associated with a number of novel transport phenomena, such as ultra-high mobility, titanic MR, and the chiral anomaly [25,30,48–52].

In contrast to DSMs and WSMs, which have zero-dimensional band crossings, NLSs have extended band crossings along special lines in k-space. Nodal lines can cross the Brillouin zone (BZ) in the shape of a closed ring or a line [53], as shown in Figure 1(c). Similar to the characteristic 1D Fermi arc surface state of WSMs, nodal ring semimetals are characterized by the 2D topological 'drumhead' surface

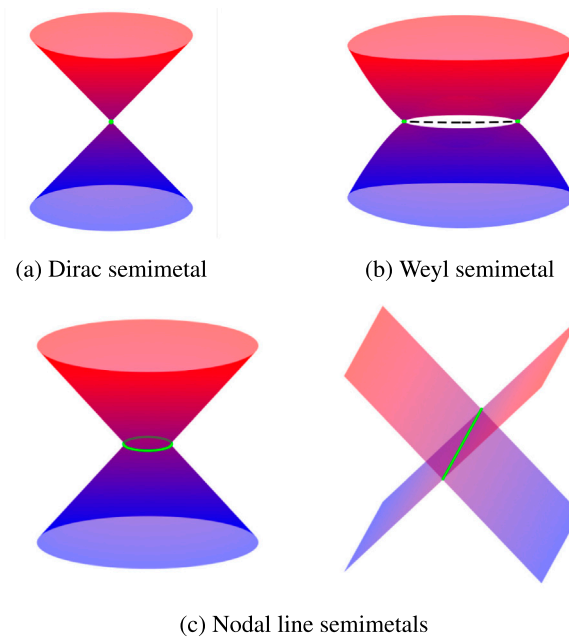(a) Dirac semimetal   (b) Weyl semimetal

(c) Nodal line semimetals

Figure 1. Schematic illustration of Dirac node, Weyl node and Nodal line/ ring in momentum space. (a) Schematic of a Dirac semimetal where the bands are linearly dispersed around the Dirac point. The Dirac point is shown by the green dot. (b) Weyl semimetal, in which the Weyl points with opposite chirality are connected by the characteristic Fermi arc. The Weyl points are shown by the green dot and Fermi arc is shown by the black dotted line. (c) Nodal line semimetals where valence and conduction bands cross along special lines in momentum space forming either a ring-shaped line or 1D line, shown by the green circle/line.

state [54]. The distinguishing characteristic of these 'drumhead' surface states is that they are embedded inside the 'direct gap' between conduction and valence bands in the 2D projection of the nodal ring [55,56]. These edge states are approximately dispersionless, analogous to the acoustic vibration on the surface of a drum, and give rise to a large density of states [57]. The flat band surface states could potentially realize high-temperature superconductivity, magnetism, or other correlated effects [57,58]. There have been several predictions of novel phenomena in Nodal line/ ring systems. In nodal ring systems, long-range coulomb interactions are expected due to a vanishing density of states at the E_F and partially screened Coulomb interaction [59]. In addition, the appearance of zero modes due to non-dispersive Landau levels is predicted to exist inside the nodal ring [60]. Nodal line systems are predicted to show a quasi-topological electromagnetic response which is related to charge polarization and orbital magnetization [61], as well as a light-induced Floquet effect in which NLS can be driven into a WSM state through a circularly polarized light [62–64].

Crystallographic symmetries play an important role in realizing TSMs. Depending on the symmetry protection, NLS can typically be categorized into two types: Dirac Nodal Line Semimetals (DNLS) and Weyl Nodal Line Semimetals

(WNLS). The DNLS are found in materials with both inversion symmetry and time-reversal symmetry. When SOC is neglected or negligibly small, band inversions happen at one or more high-symmetry points along the BZ, resulting in two doubly degenerate bands crossing each other to form a fourfold degenerate nodal line. WNLS lack either inversion or time-reversal symmetry allowing for spin slitting. Therefore, the otherwise fourfold degenerate nodal lines split into two singly degenerate nodal lines which are protected by one additional symmetry. Although it is known that certain crystalline symmetries play an important role in protecting band degeneracy [65], finding materials with stability of the degeneracy near the E_F, especially in the presence of SOC, are still one of the main goals of the field[66,67].

In the last few years, this field has gone through a lot of development, in regards to the theoretical proposals, the discovery of new materials, and the study of experimental phenomena. A number of comprehensive reviews on related topics have also came up [3,33,67–72]. This work will detail the aforementioned protection mechanisms in the context of both predicted as well as the verified NLS materials. Section 2 reviews three types of crystalline symmetries that generate NLS, including inversion plus time-reversal symmetry, mirror reflection symmetry, and non-symmorphic symmetry. The effect of SOC on these symmetry protections will also be discussed. Section 3 presents examples of materials which are observed or predicted, by these three protection mechanisms, to be NLS. Out of the currently studied materials only Pb(Tl)TaSe$_2$ and Zr(Hf)SiS have WNL and DNL's, respectively, in a real-life scenario. PbTaSe$_2$ was the only WNLS, in which two Weyl nodal rings are 0.05 eV and 0.15 eV above the E_F. It also has one accidental nodal ring created by SOC [73]. Zr(Hf)SiS, SrIrO$_3$, and IrO$_2$ have nodal ring/ line protected by non-symmorphic symmetry that are robust against SOC [66,74,75]. SrIrO$_3$, however, can gap out when magnetic ordering is included and is still being investigated [76]. All other DNLS reviewed here have nodal rings without SOC, however, including SOC turns them into Weyl semimetals or TIs. Section 4 predicts a new WNLS candidate, KCu$_2$EuTe$_4$, which, like PbTaSe$_2$, has Weyl nodal lines and rings very close to E_F in the presence of SOC. Section 5 summarizes and discusses the potential future applications of NLS.

2. Crystalline symmetries

The DNLS can be considered as a starting point for realizing many other topological states. Figure 2 shows the relationship between these different topological classes. Starting from a spinless DNLS, SOC could lift the degeneracy along the crossing line, leading to (1) a spinful DNLS when the line of degeneracy is protected by a combination of time-reversal, inversion, and non-symmorphic symmetry (i.e. ZrSiS [74,77,78]); (2) a spinful WNLS (i.e. PbTaSe$_2$ [73,79–82]) when mirror reflection within high-symmetry plane protects the nodal lines, but
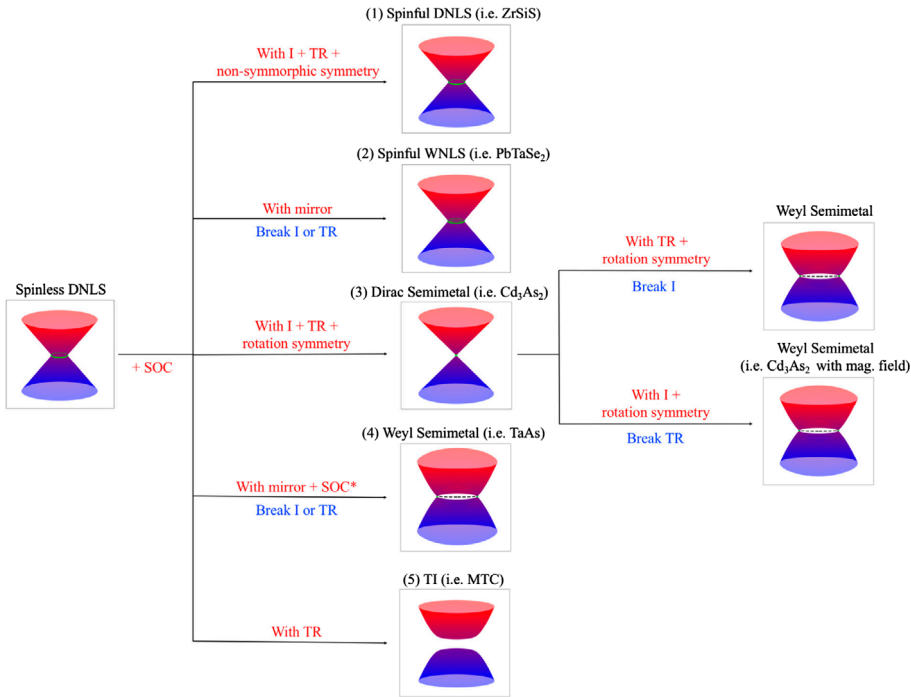
Figure 2. Schematic of different topological states and their relationship with each other. The symmetries in red (blue) caption indicate the global symmetry or spatial/ lattice symmetry elements need to be preserved (broken) to realize the new topological phase.
*This evolution to a Weyl semimetal requires 3 components: mirror reflection symmetry, atomic orbital components making up the bands forming the nodal lines, and the proper strength of SOC. If the strength of SOC is too strong, the system turns into a fully gapped insulator [85].

broken inversion symmetry (or broken time-reversal symmetry) splits the spin component at the nodal ring, giving rise to two Weyl rings; (3) a 3D DSM (i.e. Cu_3PdN [83,84]) if certain symmetry-invariant points are protected by rotation symmetry as well; (4) a WSM (i.e. TaAs [21,37]) when the system has mirror reflection symmetry, orthogonal orbital component making up the electronic states, and proper strength of SOC; and (5) a TI (i.e. Mackay-Terrones crystal [54]) if the material has only inversion and time-reversal symmetry. This would give rise to a gapped bulk state but linearly dispersed projected surface states. Starting from DSMs, breaking either inversion or time-reversal symmetry will lead to WSMs.

The symmetry of a crystal structure and the atomic orbitals making up the electronic states at band crossings determine which topological state is realized under consideration of SOC: the electronic states must be orthogonal to each other in order to not get hybridized with each other and open a gap. This means one has to consider both crystal symmetry and orbital symmetry and, when taking spins of electrons into account, to consider the number of irreducible representations in the double group. For example, the C_{2v} point group (without

spin) has four irreducible representations, but the C_2v double group (including spins) only has one irreducible representation. Since two bands with the same irreducible representation hybridize (mixing because they are not orthogonal), C_2v is gapped in the presence of SOC [86].

Global symmetry and spatial/ lattice symmetry are needed to realize NLS. Currently, three different recipes are known to yield a NLS. One is the combination of inversion and time-reversal symmetry. The second recipe is to introduce additional mirror symmetry, where the degeneracy on the mirror plane is protected. The third recipe is to introduce non-symmorphic symmetry such as glide mirror or screw rotation. The non-symmorphic symmetry demands normally singly degenerate points to cross at certain doubly degenerate points at the BZ zone boundary [86,87]. SOC plays different roles in three scenarios. In this section, these three recipes, as well as the effect of SOC on them will be discussed.

2.1. Inversion and time-reversal symmetry

In the absence of SOC, a crystalline system with simultaneous presence of time-reversal and inversion symmetries generates a DNL in 3D [83]. In such case, when the 3D block Hamiltonian is invariant under inversion and time-reversal symmetry, inversion and time-reversal symmetry constrain the Berry phase (Φ) on a closed loop in momentum space (C) to satisfy $\Phi(C) = \Phi(-C)$ and $\Phi(C) = \Phi(-C)^*$. A non-trivial loop, where $\Phi(C) = -1$, means that the loop contains a degeneracy. In 3D, this guarantees a small nodal loop at the band inversion [83].

In the presence of SOC, Dirac crossings generated with this mechanism are, in general, gapped out owing to band repulsion, unless the SOC is negligibly small, turning the system into a TI. However, if the system has an additional C_n, in particular, C_3, C_4, and C_6 rotation symmetries, the rotation symmetry can protect the band crossing at certain generic discrete points, turning the system into a DSM in the presence of SOC. Specifically, one has to consider the crystal structure and orbital symmetry in a double group along the rotation axis. If the electronic states along the rotation axis have different irreducible representations, rotation symmetry protects the Dirac points on the axis. Everything else over the BZ is gapped, thus giving rise to a 3D DSM in the SOC regime [86].

2.2. Mirror reflection symmetry

When the mirror operation and the Hamiltonian commute, nodal rings can be generated and protected by mirror reflection symmetry in the absence of SOC. For example, assuming a system described by Hamiltonian $H(k_x, k_y, k_z)$ has mirror reflection M_{xy}, one has $MH(k_x, k_y, -k_z)M^{-1} = H(k_x, k_y, k_z)$. In two high-symmetry planes, $k_z = 0$ and $k_z = \pi$, the mirror operation and the Hamiltonian commute. This makes them simultaneously diagonalizable, resulting in oppositely signed mirror eigenvalues. Therefore, without SOC, these

two bands that cross at the Dirac point are protected by the reflection symmetry from hybridizing with each other [66,67,88,89].

Taking into account of SOC, depending on the atomic orbitals making up the electronic states and the strength of SOC, SOC can turn a spinless Dirac nodal rings into (1) a spinful Weyl nodal rings within the mirror planes (i.e. PbTaSe$_2$ [73,79–82]). In this case, the WNLs are protected by mirror reflection symmetry; (2) a Weyl semimetal which has Weyl points off the mirror planes (i.e. TaAs [21,37]). These Weyl points are completely accidental, highly depends on the strength of SOC and are no longer a result of mirror symmetry. (3) a TI when the strength of SOC is strong enough (i.e. CaAgAs [85,89]).

2.3. Non-symmorhpic symmetry

To understand how non-symmorphic symmetry generates a NLS, it is important to first understand how more than one electronic unit in a unit cell, or the choice of unit cell, results in band folding. The following explanation was first laid out by Hoffman et al. [90,91]. Consider a 1D chain of molecules, one can either see it as a polymer with one atom per unit cell, or twice as many atoms per unit cell. Constructing the orbitals of the polymer with two different unit cells, when the polymer is considered to have two atoms per unit cell, as shown in Figure 3(a), it has one branch disperse upward from the bonding orbitals, and the other branch disperse downward from the antibonding orbitals. The bonding and antibonding orbitals are degenerate precisely at $k = \pi/(2a)$. When the polymer is regarded as having one atom per unit cell, the band structure is plotted in Figure 3(b) with a larger BZ.

Since the band structure of a polymer should not depend on the choice of unit cell, the two unit cell construction must result in identical band structures. In other words, the band structure in Figure 3(a) with two bands and the band structure in Figure 3(b) with one band must carry the same information about electronic bands. This could be understood in the way that the production of Figure 3(a) is Figure 3(b) being 'folded back', as the process shown in Figure 3(c). This band-folding process can be continued. If the unit cell is tripled, the band will fold as shown in Figure 3(d). If it is quadrupled, it folds like shown in Figure 3(e), and so on [90].

This is essentially what happens in non-symmorphic symmetry crystals. A non-symmorphic symmetry element $G = \{g \mid t\}$, shown in Figure 4(b), is composed of a point group symmetry operation g and a partial lattice translation t. The translation operation do not conserve spatial origin and causes enlargement of a unit cell in comparison to the symmorphic space group (comparing Figure 4(a) and (b)). The enlargement of a unit cell is analogous to the double-atom-per-unit-cell idea discussed in Figure 3, which causes the folding of k-space, and forces a band degeneracy the BZ boundary.

The band structures of non-symmorphic symmetry crystals can simply be generated by the folding back procedure. Given the two unit cells in Figure 4(a)
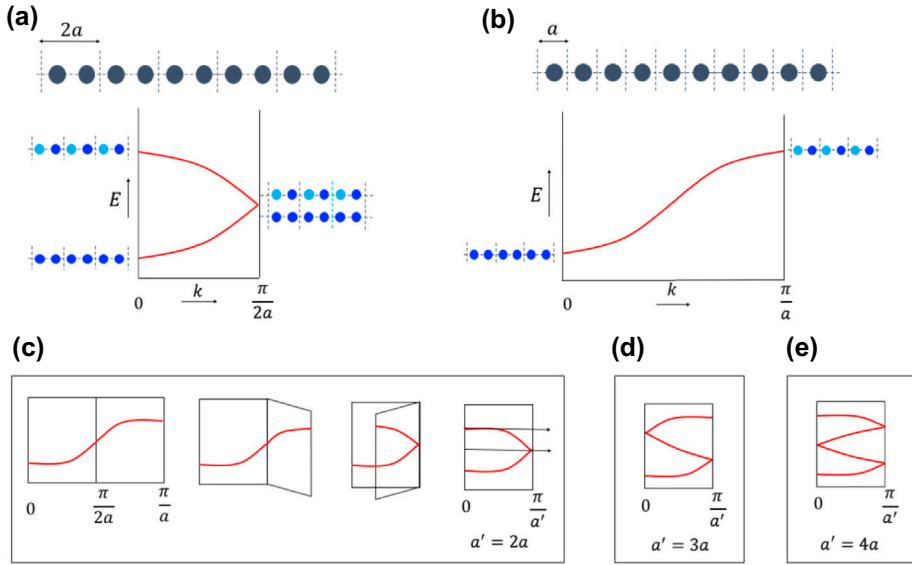
Figure 3. Band folding in one-dimensional polymers. (a) Band structure of a polymer in which there are two atoms per unit cell. The bands contain two branches: one from the 'running up' bonding bands, and one from the 'running down' antibonding bands. The two branches intersect at $k = \pi/(2a)$. (b) Band structure of a polymer in which there is one atom per unit cell. The BZ is doubled because the unit cell is one half as it is in (a). (c) Production of band structure in (a) by folding band structure in (b). (d)–(e) Enlargement of the unit cell causes the multiplicity of bands. Bands are folded three times when the unit cell is tripled, four times when quadrupled.

and (b), one can construct the corresponding BZ as shown in Figure 4(c), where the BZ of the symmorphic square lattice is shown in green and that of non-symmorphic square lattice is shown in red. The green-shaded area I can be translated back to the green-shaded area II, which is equal to the red-shaded area by time-reversal symmetry because time-reversal symmetry implies $E_n(k) = E_n(-k)$. Since X lies exactly at the midpoint of $\Gamma - M'$, and also of $M - X'$, folding the $\Gamma - X' - M' - M$ square in half across the $M - X'$ diagonal like a sheet of paper, one can see that $X - M'$ folds directly onto $\Gamma - X$. Similarly, $X' - M'$ folds onto $\Gamma - X'$. In addition, $\Gamma - X'$ is equivalent to $\Gamma - M$, thus explaining the band structure in Figure 4(e) as a simple folding of Figure 4(d) [91]. In particular, $\Gamma - X$ of the non-symmorphic square can be constructed by folding $\Gamma - M'$ of the symmorphic square lattice in half, and Γ–M (which is equivalent to $\Gamma - X'$) of the non-symmorphic square can be constructed by the superposition (caused by the folding) of $\Gamma - X'$ and $X' - M'$ of the symmorphic square lattice [91].

What is interesting about the non-symmorphic-protected nodal lines is that they cannot be gapped by SOC because they are protected by a lattice translation [87]. Take glide mirror as an example, since the translation t is a fraction of a primitive unit vector, in spinless systems for Bloch states at k, $G^2 = e^{-i\mathbf{k}\cdot\mathbf{t}}$. Therefore, the glide eigenvalues are $\pm e^{-i\mathbf{k}\cdot\mathbf{t}/2}$. Considering spins, the glide eigenvalues are $\pm i e^{-i\mathbf{k}\cdot\mathbf{t}/2}$. Either with or without SOC, the non-symmorphic
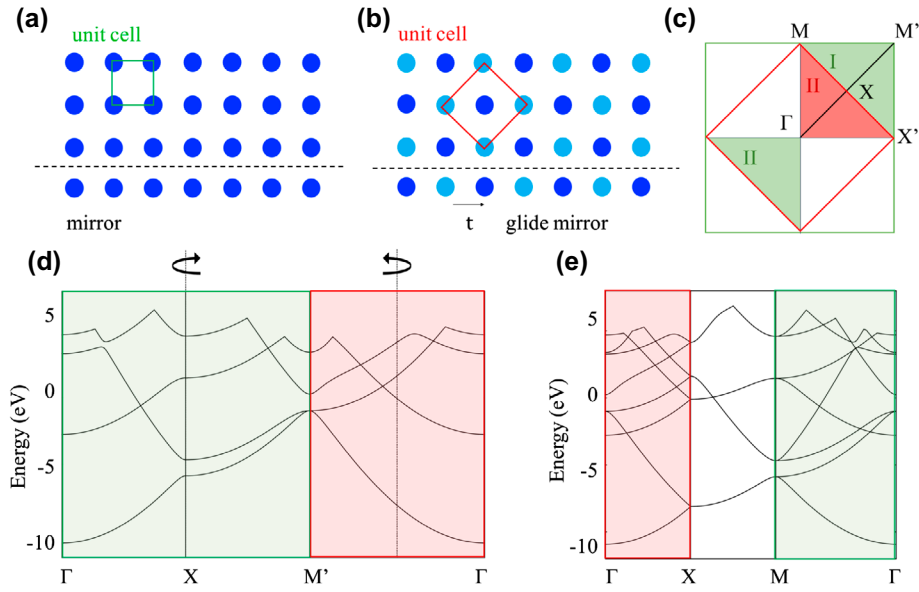
Figure 4. Band folding in two-dimensional square lattice. (a) Symmorphic square lattice with mirror reflection symmetry, in which the unit cell is shown in green. (b) Non-symmorphic square lattice with glide symmetry. The unit cell shown in red is larger than the unit cell of symmorphic square lattice. (c) The BZ of the symmorphic and non-symmorphic square lattices, which are enclosed by green and red lines, respectively. The green-shaded area I is equal to the green-shaded area II by translation, which is also equivalent to red-shaded area II by time-reversal symmetry. (d)–(e) The band structure of non-symmorphic square lattice (e) can be obtained from the band structure of symmorphic square lattice (d). Folding the square made by $\Gamma - X' - M' - M - \Gamma$ along M–X' makes M' coincide with Γ. Therefore, $\Gamma - X$ of the non-symmorphic lattice can be obtained by folding $\Gamma - M'$ of the symmorphic square lattice in half. Similarly, the same folding makes X'–M' superimpose onto $\Gamma - X'$ which is equivalent to $\Gamma - M$ of the non-symmorphic lattice. The dashed lines show folding points of the symmorphic band structure.

symmetry give two distinct eigenvalues, therefore the bands are protected from being hybridized [88].

3. Material realization

3.1. Time-reversal and inversion symmetry-protected nodal line materials

Centrosymmetric materials have inversion symmetry. If time-reversal symmetry is also presence in the system, fourfold degeneracies along nodal rings can be realized. Nodal rings created in this way generally exist only in the limit of vanishing SOC. Including SOC typically turns the DNLS into either a DSM or a TI. Some predicted centrosymmetric DNL materials include cubic antiperovskite materials Cu_3NX [83,84], CaTe [92], LaX [93], Ca_3P_2 [94], CaP_3 family [95], $BaSn_2$ [96,97], AlB_2-type diborides [98–100], and 3D carbon allotrope materials with negligible SOC such as Mackay-Terrones crystals [54] and hyperhoneycomb lattices [101]. In addition, two-dimensional DNL materials have also been proposed in monolayer Cu_2Si [102] and honeycomb-kagome lattice [103].

Tables 2 and 3 show the crystal structures, electronic band structures without and with SOC, as well as nodal line distributions without SOC within a BZ. Without SOC, the Dirac points responsible for the nodal lines are coded with red square box in the band structure. With SOC, all three compounds shown in Table 1 turn into DSM. All the other compounds shown in Tables 2 and 3 are gapped into TIs (except TiB_2). The Dirac points of DSM with SOC are coded with red square box in their corresponding band structures. Nodal lines without SOC within a BZ are shown in red lines, and the high-symmetry lines are shown in black lines together with high-symmetry points.

Cu_3NX [83,84]: Cu_3N crystallizes in the cubic anti-RuO_3 structure in space group $Pm\bar{3}m$ No. 221. At the center of the unit cell there is a void, which can host intercalate atoms such as Ni, Cu, Pd, An, Ag, and Cd. By doping it with extrinsic non-magnetic atoms, a Dirac nodal ring occurs near the E_F without SOC. As an example, Cu_3NPd is an antiperovskite material (shown in Table 1) in which the conduction and valence bands are inverted at the R point. Without SOC, the bands are six-fold degenerate around R, forming three nodal rings perpendicular to each other. When SOC is included, C_4 symmetry along the R-M line protects the Dirac point on the line, making Cu_3NPd, in reality, a 3D DSM with three pairs of Dirac points. Since the heavy Pd in Cu_3NPd brings a large SOC, the effect of SOC can be diminished by replacing Pd with lighter elements such as Ag and Ni.

CaTe [92]: CaTe is a CsCl-type structured alkaline-earth chalcogenide also in space group $Pm\bar{3}m$ No. 221. Without SOC, CaTe is a topological nodal ring semimetal: three nodal rings are perpendicular to each other at M point with the drumhead surface states embedded within each ring (Table 1). When SOC is considered, each nodal ring evolves into two Dirac points along the M-R line, which are protected by the C_4 rotation symmetry, making CaTe a 3D DSM.

LaX [93,97,104–107]: The family of lanthanum monopnictides LaX has the rock salt structure, where X could be N, P, As, Sb, or Bi. It is in space group Fm-$3m$ No. 225 (shown in Table 1). When SOC is ignored in LaN, band crossings form three intersecting nodal rings centered at the X point, which are protected by inversion symmetry, time-reversal symmetry, as well as C_4 rotation symmetry. When SOC is considered, spin rotation symmetry is broken, resulting in a lift of degeneracy everywhere except two Dirac points. Therefore, SOC turns the nodal rings into three sets of Dirac points at three X points. However, the other compounds in the pnictogen group are TIs with SOC because of larger lattice constant and enhanced SOC [93].

Although the DFT calculations show the compounds in the LaX family other than LaN to be TIs with SOC, some recent transport measurements indicate that they behave like semimetals [104–106]. In particular, both LaSb and LaBi show extreme MR, which are possibly originated from a combination of electron-hole compensation and a special orbital texture on the electron pocket [104,105]. Their anisotropic characteristic of MR is the result of ellipsoidal electron pockets
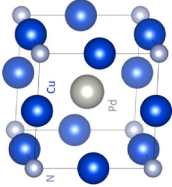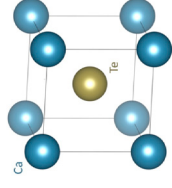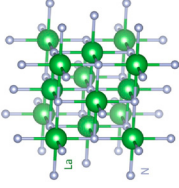
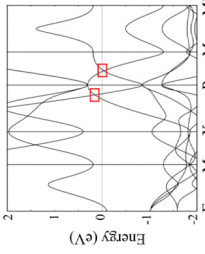**Table 1.** Centrosymmetric nodal line materials.
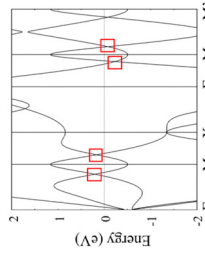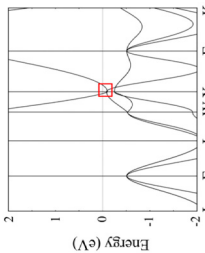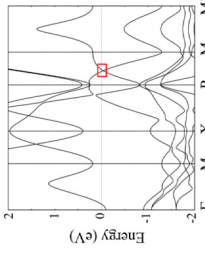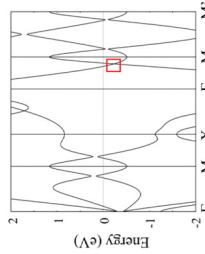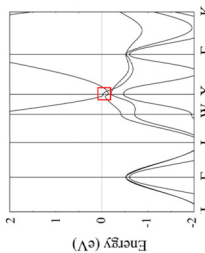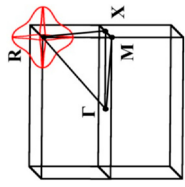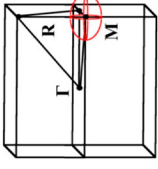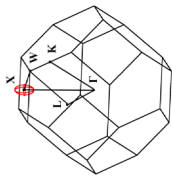
Materials	Cu$_3$NPd	CaTe	LaN
Crystal structure			
Band structure without SOC			
Band structure with SOC			
Nodal line distribution without SOC			
References	[83,84]	[92]	[93,97,104–107]

Table 2. Time-reversal and inversion symmetry-protected nodal line materials (continued).

Materials	Ca_3P_2	$BaAs_3$	$BaSn_2$	TlB_2
Crystal structure				
Band structure without SOC				
Band structure with SOC				
Nodal line distribution without SOC				
References	[89,94]	[95]	[96,97]	[98–100]

centered at the X point [106]. However, ARPES measurements show that LaSb is topological trivial without any surface state observed [107], and LaBi with an usual surface state which has a linear conduction band and a parabolic valence band [108].

Ca_3P_2 [89,94]: Ca_3P_2 has the hexagonal Mn_5Si_3-type crystal structure with space group $P6_3/mcm$ No. 193 (shown in Table 2). Without SOC, Ca_3P_2 shows a fourfold degenerate nodal ring. Band crossings are protected by $k_z=0$ mirror plane and a combination of inversion and time-reversal symmetry. The SOC is very small for the light elements Ca and P and when SOC is included, spin-rotation symmetry is conserved resulting in a very small band gap opening in the crossing of Ca_3P_2.
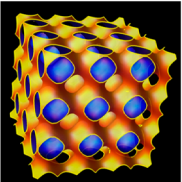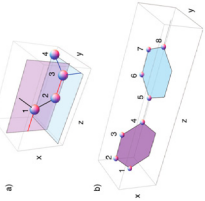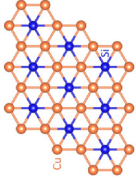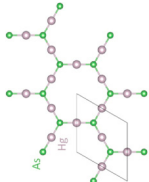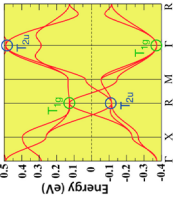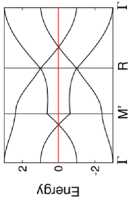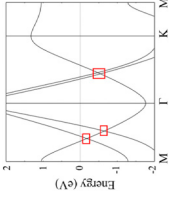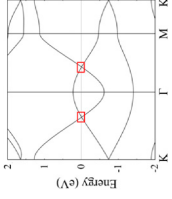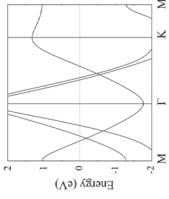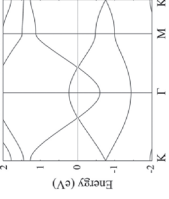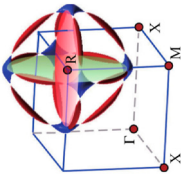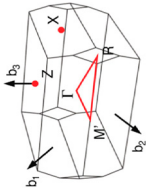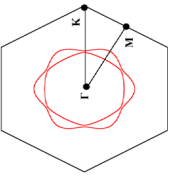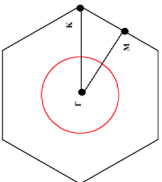
CaP_3 family [95]: The crystal structure of CaP_3 families (CaP_3, $CaAs_3$, SrP_3, $SrAs_3$, and $BaAs_3$) can be seen as a series of 2D puckered polyanionic layers stacking on top of each other: within each layer, 14 P atoms form a 2D circle, with 2 Ca atoms sitting inside the circle; in between the layers, different layers stack along the b axis. Among the CaP_3 family of materials, CaP_3 and $CaAs_3$ belong to space group $P\bar{1}$; SrP_3, $SrAs_3$, and $BaAs_3$ belong to space group $C2/m$. The family has both inversion and time-reversal symmetry. Without SOC, the conduction and valence bands with opposite eigenvalues are inverted around Y point near the E_F, giving rise to the nodal lines for SrP_3, $SrAs_3$, and $BaAs_3$ at the Γ–Y–S plane, and the nodal lines for CaP_3 and $CaAs_3$ slightly off the plane. Taking into account of SOC, all the crossings are gapped along the nodal line, making them TIs. Among all materials within the family, SrP_3 gives the smallest gap (6.11 meV along S–Y and 1.76 meV along Y − Γ). Table 2 shows an example of $BaAs_3$. The SOC induced gap in $BaAs_3$ is 38.97 meV along S-Y direction and 6.22 meV along Y–Γ direction.

Alkaline-earth stannides, germanides, and silicides [96,97]: The alkaline-earth AX_2 family of compounds have similar crystal and electronic structures. $BaSn_2$ (Table 2), for example, crystalizes in the trigonal structure. It is in space group $P\bar{3}m1$ No. 164. In $BaSn_2$, Sn atoms form a honeycomb lattice and the Ba layer intercalates between two adjacent Sn layers. When SOC is ignored, these materials are characterized by a snakelike closed nodal ring winding around the A point, extending above and below the $k_z = \pi$ plane. The nodal ring is protected by a combination of inversion and time-reversal symmetry. The special shape of the nodal line is determined by additional symmetries, such as the C_2 operation along A-H and the C_3 rotation symmetry along K_z. $BaSn_2$ has only one nodal ring within the BZ; most other nodal ring systems typically have multiple circles or ellipses. When SOC is included, the nodal line is gapped and the system becomes a TI.

AlB_2-type diborides [98–100]: Both TiB_2 and ZrB_2 crystallize in centrosymmetric-layered hexagonal structure with space group P6/mmm No. 191 (Table 2). It consists graphene-like boron layers and alternating hexagonal titanium or zirconium layers. Both compounds have been successfully synthesized in laboratory

Table 3. Time-reversal and inversion symmetry-protected nodal line materials (continued).

Materials	MTC	Hyperhoneycomb lattice	Cu$_2$Si	Hg$_3$As$_2$
Crystal structure [101]				
Band structure without SOC [54,101]				
Band structure with SOC	N/A			
Nodal line distribution without SOC [54,101]		N/A		
References	[54]	[101,111,112]	[102]	[103]

and have brought much interests owing to the unique combination of properties such as high melting point, high bonding strength, high thermal, and electrical conductivity [109,110].

Some electronic properties of the AlB_2 diborides are embedded in their band structures, such as a nodal net structure including triple point, nexus, and nodal link [98,99]. Take TiB_2 as an example, without SOC, six band crossings emerge around the E_F, along the H-Γ, Γ–A, A–H, K–Γ, M-K, and L-A directions. These band crossings give rise to four different kinds of nodal line structures, including 1) a nodal ring in the M_xy plane centered around K point [100]; 2) a nodal ring in the in the M_xy plane centered around A point; 3) nodal lines in three vertical mirror planes σ_{v1}, σ_{v2}, and σ_{v3}; and 4) nodal line along Γ–A starting from a triple point. All the four classes of nodal lines together compose a complex nodal net structure. In the presence of SOC, all the crossings except the one along Γ–A are gapped out, with the gap size ranging from 18 meV to 26 meV. SOC also generates a new Dirac point along Γ–A.

Mackay-Terrones crystal [54]: A Mackay-Terrones crystal (MTC) is a 3D network formed by tessellation of 4, 6, or 8 member carbon rings on top of a primitive Schwarz minimal surface. Table 3 shows a 6-membered example with space group $Pm\bar{3}m$. Without SOC, the coexistence of spacial inversion and time-reversal symmetry generate and protect three orthogonal nodal rings. The nodal rings are in the $k_x = \pi/a$, $k_y = \pi/a$, and $k_z = \pi/a$ planes around the R point. Nodal line distributions in Table 2 show the electron pockets contribution (in blue) and hole pocket contribution (in red) to the nodal lines. Including SOC, a gap opens up leading to a 3D TI. However, similar to graphene, the computed SOC is very small (around 0.13 meV at 1.5 K).

3D Honeycomb lattice [101,111,112]: A 3D honeycomb lattice is a 3D analog to a 2D honeycomb lattice. Two typical 3D honeycomb lattices include the hyperhoneycomb and stripy-honeycomb lattice, which can be realized in β–Li_2IrO_3 and γ–Li_2IrO_3, respectively [113–115]. Both of these lattices have been predicted to host nodal loops without SOC. For example, in the hyperhoneycomb lattice, shown in Table 3, all atoms are connected by three coplanar bonds spaced by 120 degrees. The planar trigonal connectivity of sites and its sublattice symmetry give rise to Dirac nodes. A tight-binding model reveals the Fermi surface to be a highly anisotropic torus shape and is expected to show quantized Hall conductivity when applying magnetic field along the torus direction [101]. Various antiferromagnetic (AFM) orders are reported in the hyperhoneycomb lattice [116–118], some of which can destroy the nodal loop [111]. Including SOC in these systems, regardless of magnetism, evolves them into strong TIs [101,111].

Cu_2Si [102]: Cu_2Si is composed of a honeycomb Cu lattice and a triangular Si lattice, in which Si and Cu atoms are coplanar in monolayer (Table 3). It is in space group $P63/mmc$ No. 194. Without SOC, the Dirac nodal rings in Cu_2Si are shown as two concentric rings centered at Γ point. Introducing buckling in the

Cu lattice, shifting Si atoms out of plane, or artificially increasing the strength of SOC gaps out the nodal ring, confirming that mirror symmetry protects the Dirac nodal ring in the absence of SOC. However, because SOC is intrinsically small in Cu_2Si, its effect is also small (gap openings ≤ 15 meV). Unlike many other proposed materials which are hard to synthesize, especially in thin film form, the experimental synthesis of monolayer Cu_2Si on Cu(111) surface by chemical vapor deposition has been realized decades ago, and ARPES has been measured confirming the band crossings at both sides of Γ [102].

Honeycomb-kagome(HK) lattice [103]: HK lattice is a composite lattice composed by interpenetrating honeycomb and kagome sublattices. It can be realized in A_3B_2 compounds where A is a group-IIB cation and B is a group-VA anion. A_3B_2 compounds have been predicted to host a 2D nodal ring. For example, in Hg_3As_2 (Table 3) with space group $P63/mmc$ No. 194, a band inversion happens between the Hg s-orbital and the As p_z-orbital without SOC. With respect to xy mirror plane, the eigenstates of two bands have same parity but opposite eigenvalues, therefore resulting in a band inversion. In the presence of SOC, the nodal ring turns into a 2D TI, which has been confirmed by the existence of non-trivial helical edge states [103].
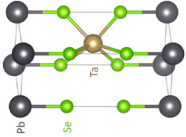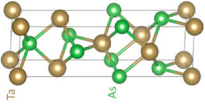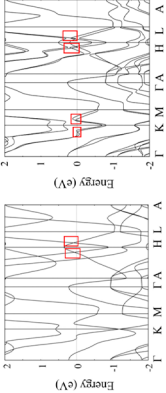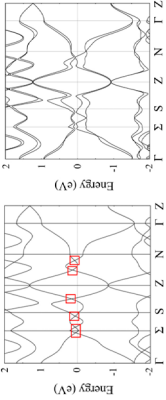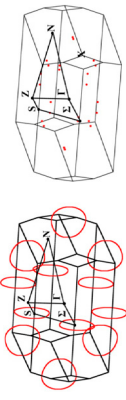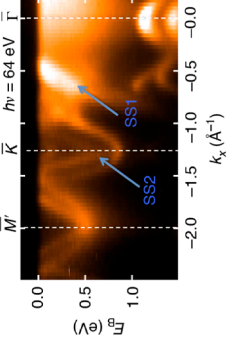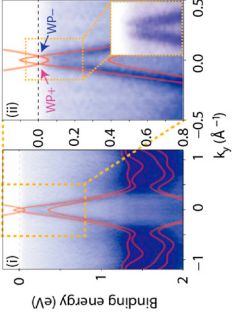
3.2. Mirror reflection symmetry-protected nodal line materials

When a material has a mirror reflection symmetry which commutes with its Hamiltonian, without SOC, nodal lines can be generated by the mirror operation. With SOC, depending on the strength of SOC as well as the atomic orbitals making up the electronic states, the spin degeneracy can be lifted, evolving a DNLS into a WNLS ($PbTaSe_2$), a WSM (TaAs and HfC), or a TI ($CaAgX$($X =$ P, As)). These three classes are discussed below in this section.

Tables 4–5 show the crystal structures, electronic band structures without and with SOC, nodal line (Weyl points) distributions without and with SOC within a BZ, as well as the available ARPES measurements confirming the presence of nodal lines (Weyl points). Without SOC, the Dirac points corresponding to the nodal lines are coded with red square boxes in the band structure. With SOC, the red square boxes indicate the mirror symmetry-protected crossings and SOC-created accidental crossings. The nodal line distribution without SOC, as well as the nodal line/ Weyl points distributions with SOC are also shown in the tables.

Pb(Tl)TaSe$_2$ [73,79–82,119–121]: $PbTaSe_2$, shown in Table 4, is a layered, non-centrosymmetric compound in space group P-$6m2$ No.187[79]. Specific heat, electrical resistivity, and magnetic susceptibility, London penetration depth measurements have shown it to be a anisotropic type-II BCS superconductor [79,119–121]. The crystal structure of $PbTaSe_2$ can be thought of as alternating stacks of $TaSe_2$ and hexagonal Pb layers, with Pb atoms directly sitting above the Se atoms. It contains a mirror plane going through the Ta atomic plane that reflects k_z to $-k_z$, which plays the essential role in protecting the topological nodal line.
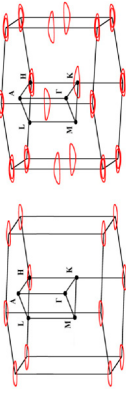
Table 4. Mirror reflection symmetry-protected nodal line materials.

Materials	PbTaSe$_2$	TaAs
Crystal structure		
Band structure without and with SOC		
Nodal line distribution without and with SOC		
ARPES [37,73]		
References	[73,79−82], [119−121]	[21,30,35−38,40,48,52,122−129]

Without SOC, the conduction and valence bands of both Pb and Se belong to different representations with opposite eigenvalues, forming spinless nodal rings around H and H′ in the plane of $k_z = \pi$. When SOC is included, due to the spin degeneracy being lifted because of the lack of inversion symmetry, each band splits into two bands with opposite spin polarization and mirror reflection eigenvalues. Consequently, the spinless Dirac nodal ring turns into four spinful Weyl nodal rings. Of these four spinful nodal rings, only two are protected by mirror reflection, resulting in two nodal rings around H protected by the reflection symmetry with respect to Ta atom plane. In addition, SOC also gives rise to another accidental crossing generating a nodal ring at the K point on the $k_z=0$ plane that does not exist without SOC. The ARPES measurements (Table 4) along M-K-Γ show the nodal ring around K point, with the surface states (SS) indicated by the blue arrows [73,81]. This represents a rare case where SOC creates a Weyl nodal ring by generating 'new' crossings rather than by just splitting Dirac nodal rings apart. It also serves as a good example that systems with 2D massive Dirac fermions can be interfaced with a transition metal dichalcogenide to create thermodynamically stable 3D massive Dirac fermions.
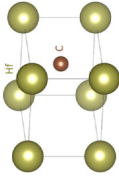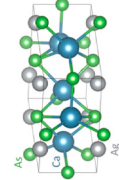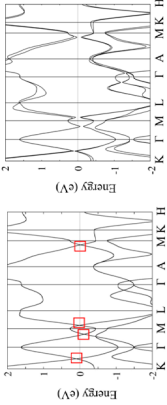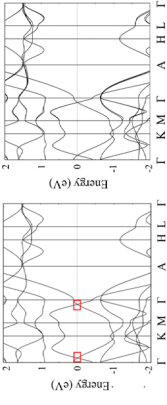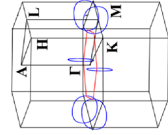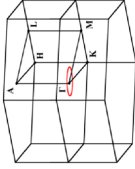
Aside from the mirror reflection protected and the accidental band crossing-generated nodal lines, spin momentum locked spin texture is another interesting feature of PbTaSe$_2$, as it is one of the most prominent characteristics of topological surface states [80,81]. Two superconducting topological surface state (TSS) have been predicted by DFT calculations with opposite helical spin polarization existing within the bulk gap at Γ and have been confirmed by quasiparticle scattering interference results [80]. The fully gapped superconducting order of the TSSs in the presence of helical spin polarization make PbTaSe$_2$, and related compounds, promising candidates to be topological superconductors.

TaAs family [21,30,35–38,40,48,52,122–129]: TaAs is in a body-centered tetragonal structure with non-symmorphic space group $I4_1md$ No. 109, which lacks inversion symmetry (Table 4). Its structure can be thought of as planes of face-sharing trigonal prisms stacked on top of each other but rotated by 90 degrees every layer. It contains two mirror planes, M_x and M_y, and two glide planes, M_xy and M_{-xy}.

Without SOC, band crossings within the ZNΓ plane are protected by M_y because of the opposite mirror eigenvalues, therefore creating nodal rings within the plane. It is important to note here that although TaAs also has glide mirrors, the non-symmorphic mirror operations do not generate the crossings in this system. Including SOC, the nodal rings within the ZNΓ plane are fully gapped, resulting in two pairs of Weyl points located 2 meV above the E$_F$ and four pairs of Weyl points located about 21 meV below the E$_F$. All Weyl points are located slightly off the mirror planes.

After the theoretical prediction of this Weyl semimetal family (TaAs, TaP, NbAs, and NbP), a series of photoemission, tunneling spectroscopy, and transport measurements have been carried out to probe the characteristic of Weyl

Table 5. Mirror reflection symmetry-protected nodal line materials.

Materials	HfC	CaAgAs
Crystal structure		
Band structure without and with SOC		
Nodal line distribution without and with SOC		TI with SOC
References	[85]	[130]

fermions. These include the observation of Fermi arcs by ARPES [35–38,40,122] and by scanning tunneling microscope (STM) [123,124]. For example, Table 4 shows an an ARPES measurement of a broadband dispersion (i) and a zoomed-in plot (ii) across the two Weyl points, denoted by WP+ and WP−.

The linear band dispersion and non-trivial Berry phase are characterized by chiral magnetotransport properties, such as ultra-high mobility, large transverse MR [52,125–128], and negative longitudinal MR [30,48,126,127,129], and the studies of chiral magnetotransport properties [30,48,52,126,127].

HfC [85]: The WC-type HfC is in hexagonal space group $P\bar{6}m2$ No. 187 (Shown in Table 5). It has time-reversal symmetry and two mirror planes, including $M_{x}y$ and $M_{x}z$, but lacks inversion symmetry. Protected by mirror symmetry $M_{x}y$ and $M_{x}z$, two types of nodal rings emerge in the absence of SOC, one lying in the $M_{x}y$ plane around the Γ point, and the other one lying in the $M_{x}z$ plane around the M point. With SOC, the crossings along Γ–M, M-L, and M-A are fully gapped, split the nodal chain into 30 pairs of Weyl points off the mirror planes.

CaAgX(X**=P, As**) [130]: CaAgX crystallizes in the ZrNiAl-type structure with space group $P-62m$ No. 189 (Table 5). The AgX_4 is in kagome-triangular lattice, which is formed by edge- and corner-sharing tetrahedra with intercalated Ca atoms. It has mirror reflection symmetry ($M_{x}y$) but lacks inversion symmetry. Without SOC, the bulk DNL is protected by $M_{x}y$, creating a nodal ring around the Γ point in the BZ. Turning on SOC, the degeneracy in dihedral point group symmetry is lifted, transforming the system into a TI. For CaAgP, however, the effect of SOC is expected to be less than 1 meV [130].

3.3. Non-symmorphic symmetry-protected Dirac nodal line materials

Non-symmorphic symmetry is a global symmetry that is robust against SOC. As discussed earlier, non-symmorphic symmetry creates band folding, resulting in otherwise singly degenerate points to cross at certain doubly degenerate points at the BZ boundaries.

Tables 6–7 show the crystal structures, electronic band structures without and with SOC, nodal line distributions without and with SOC within a BZ, as well as the available ARPES measurements confirming the presence of non-symmorphic symmetry-protected nodal lines and gapped unprotected nodal lines. In the electronic band structure figures, the Dirac points corresponding to the symmorphic symmetry-generated nodal lines are coded with red square boxes, and those protected by non-symmorphic symmetry are coded with green squares (ovals). In the nodal line distribution figures, the nodal lines generated by symmorphic symmetry are shown in red lines, and those generated and protected by non-symmorphic symmetry are shown with green lines. Only non-symmorphic symmetry-generated nodal lines survive in the presence of SOC.

M**SiS** [74,77,78,87,131–138]: Zr(Hf)SiS is a tetragonal PbFCl-type compound with space group $P4/nmm$ No. 129. It has a two-dimensional layered structure

consisting of Zr(Hf) and two neighboring S layers sandwiched between Si layers. The square nets of Si atoms are located on a glide plane (Table 6).

The band structures without and with SOC clearly show that the DNL generated by non-symmorphic symmetry of the square lattice explained earlier is protected from gap opening even in the presence of SOC [87]. The bands responsible for the crossings linearly disperse as high as 2 eV above and below the E_F, which is a much larger range compared with the other known Dirac materials. For ZrSiS, without SOC, several Dirac-like crossings can be observed along Γ–X, Γ–M, Z–R and Z–A, and are protected by C_2v. The nodal loop generated by these crossings is shown in red in Table 6. In addition, there are two other Dirac crossings at the X and R points, which are located 0.7 eV and 0.5 eV below the E_F as well at M and A, located at 2.3 eV below the E_F. These crossings, shown by the solid green and light blue lines in nodal line distribution without SOC in Table 6, are located within the glide mirror planes, protected by the non-symmorphic symmetry. With SOC, the C_2v point group allows only one irreducible representation, and therefore gaps out the Γ–X, Γ–M, Z–R and Z–A crossings in both ZrSiS and HfSiS. However, the non-symmorphic-protected crossings at M, X, A, and R are robust against SOC, although these are buried below the E_F.

The non-symmorphic symmetry-protected and the unprotected symmorphic DNL have been verified experimentally by ARPES in the MSiS compound family [74,77,78,131]. In ZrSiS, the DNL protected by non-symmorphic symmetry can be clearly seen at X-R 0.5 eV below the E_F. The Dirac points (DP) responsible for the non-symmorphic nodal lines are shown with red arrow in ARPES data in Table 6 [74,77,78]. Similarly, the non-symmorphic symmetry-generated DNL was also been measured in HfSiS [78,131]. However, the C_2v-protected DNL along Γ–X and Γ–M are gapped out by SOC in both materials. Consistent with the electronic calculation, the SOC splitting is larger in HfSiS (80 meV) compared with ZrSiS (15 meV). In addition, larger Rashba splitting has also been seen at the time-reversal invariant X point in HfSiS [131], likely due to the heavier atomic mass of Hf compared to that of Zr.

Extraordinary magneto-electronic transport phenomenon have been found in this material system [132–136,138]. The MR is large and positive for both materials, reaching 1.8×10^5 percent at 9T and 2K for ZrSiS without saturation [133–135,138]. The MR are both highly anisotropic and both compounds show a 'butterfly'-shaped angular MR, originating from the 2D and 3D Dirac pockets comprising Fermi surface [132,136,138]. In addition, ZrSiS also shows evidence of a topological phase transition with changing magnetic field angle [132].

ZrSiS and HfSiS are two well-studied examples in the larger ternary material family, WHM, (W=Zr, Hf, or La; H=Si, Ge, Sn, or Sb; M=O, S, Se, and Te) [141–143], which share the same crystal structure and have topological non-trivial phases. For example, ZrSiTe has the non-symmorphic crossings at X and R lie

Table 6. Non-symmorphic symmetry-protected nodal line materials.

Materials	ZrSiS	HfSiS
Crystal structure		
Band structure without and with SOC		
Nodal line distribution without and with SOC		
ARPES [78]		
References		[74,77,78,87,131−138]

very close to the E_F, making it a good candidate system to study non-symmorphic line nodes [137].

Orthorhombic perovskite iridates [66,67,76,139,144–151]: AIrO$_3$, where A is an alkaline-earth metal, is a class of orthorhombic perovskite iridates in space group *Pbnm* No. 62. A typical unit cell of AIrO$_3$ has four Ir atoms with different oxygen octahedral environments. It contains three different mirror planes: b-glide, n-glide, and M_z.

Taking SrIrO$_3$ as an example (shown in Figure 7), without SOC, singly degenerate DNL are presence along U-R. In the presence of strong SOC from Ir, a Dirac double nodal ring emerges around the U point close to the E_F, protected by n-glide non-symmorphic symmetry. The double nodal ring exhibits a non-trivial topology that leads to localized surface zero mode protected by chiral (a combination of time-reversal and particle-hole symmetry [152]) and mirror reflection symmetry, and a pair of counter-propagating helical modes localized in a dislocation line, making it a topological crystalline metal (TCM) [144]. A direct observation of nodal lines in this correlated oxide system is still under investigation [76]. When the n-glide symmetry is broken, for example, by epitaxy-induced symmetry breaking, the double-nodal line breaks into two Dirac points [67,147]. When considering magnetism, the Dirac nodal ring evolves into a Weyl nodal ring, Weyl points, or a TI, depending on the direction of the field [144].
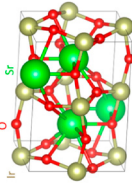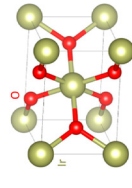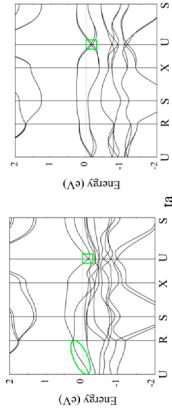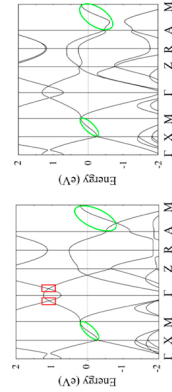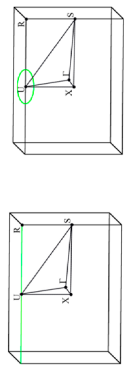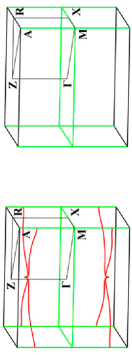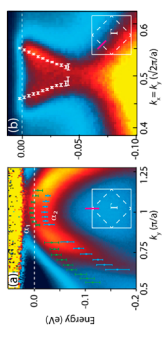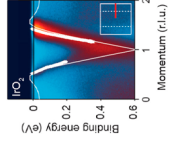
Unusual magnetotransport properties are expected to arise from such topological transitions. However, the MR of the epitaxially grown thin films are shown to be small [149–151]. One study on strain-free bulk SrIrO$_3$ shows the quadratic transverse and linear longitudinal MR to be 100 percent and 50 percent at 14 T and 2 K, which are 2 to 3 orders of magnitude higher than the MR on strained thin films [148]. Furthermore, a change in optical conductivity spectra induced by interband transition of Dirac cones has been observed. Such filed-induced topological transition of Dirac nodes could be a result of enhanced paramagnetic susceptibility [148].

Rutile oxides [75,140,153,154]: RO$_2$, where R could be Ir, Os, and Ru, crystalizes in rutile-type lattice structures in space group P4$_2$/mnm No. 136. It has one R atom sitting at each corner of a unit cell, as well as one R atom at the center. Each R atom is surrounded by six O atoms that form a distorted octahedron. Rutile oxides have both inversion and time-reversal symmetry. They also have mirror reflection symmetry $M_y z$ and $M_x y$, fourfold rotation symmetry $C_4 z$, as well as non-symmorphic symmetry n_x and $n_4 z$. Two types of DNLs exist in this system, which will be discussed below.

The first type of DNLs exist only in the absence of SOC. Without SOC, sixfold- and eightfold-crossing points appear along Γ–Z and M-A directions, which are denoted as hexatruple point (HP) and octuple point (OP). The HP and OP points are connected by DNLs inside the BZ, forming a network as shown in blue in Table 7. These nodal line networks exist in the mirror reflection planes (110)

Table 7. Non-symmorphic symmetry-protected nodal line materials (Continued).

Materials	SrIrO$_3$	IrO$_2$
Crystal structure		
Band structure without and with SOC		
Nodal line distribution without and with SOC		
ARPES [139,140]		
References	[66,67,76,139,144–150]	[75,140,153,154]

and ($\bar{1}$10). They are protected by mirror reflection symmetry without SOC and can be transformed to each other by either inversion or time-reversal symmetry. With SOC, both HPs and OPs got gapped out, as well as the DNLs connecting them.

The second type of DNLs are stable against SOC, because of the non-symmorphic symmetry. As discussed earlier, the combination of inversion and time-reversal symmetry give rise to doubly degenerate crossings considering spins. In addition, the existence of non-symmorphic symmetry generates even higher degeneracies at some specific k point in the BZ. For example, in IrO_2 (Table 7), without SOC, $k_x = \pi$ and $k_y = \pi$ appear to be Dirac nodal planes. With SOC, the combination of inversion, time-reversal symmetry, mirror reflection symmetry as well as non-symmorphic symmetry guarantees four degenerate orthogonal eigenstates along both the X-M and M-A direction. DNLs protected by non-symmorphic symmetry in IrO_2 are at the E_F, which are possibly the reason for the high conductivity and large MR in the system [153,154].

4. KCu_2EuTe_4: a new mirror symmetry-protected WNL

KCu_2EuTe_4 is one of the large family of Te square net compounds and its crystal structure is shown in Figure 5(a). Crystallizing in the tetragonal space group *P4mm* No. 99, it can be built up in the following way: layers of corner-sharing $EuTe_8$ square anti-prisms stack in edge-sharing manners with tetrahedral $CuTe_4$ layers below and square anti-prismatic KTe_8 layers above. The result is a non-centrosymmetric structure with several square nets and a particularly dense Te-square net shared by the KTe and EuTe layers. This lack of inversion, unlike the ZrSiS family of compounds, allows SOC to lift the spin degeneracies. KCu_2EuTe_4 has two sets of mirror planes, M_x and M_xy, as well as C_4 rotation symmetry, which are responsible for creating the nodal line/rings in this compound explained below.

The overview of the band structures of KCu_2EuTe_4 in the paramagnetic state without and with SOC are shown in Figure 5(b) and (c). As expected for square net compounds, without SOC, highly linearly dispersive bands are observed to cross the E_F and almost exclusively create the Fermi surface. Among them, one set of conduction and valence bands with opposite parity invert nearly at the E_F, resulting in four two-fold spinless DNL protected by M_xy mirror symmetry. The distribution of this set of nodal lines in the first BZ is shown in red in the upper panel of Figure 5(d). The energy dispersion of these nodal lines are almost flat.

Upon introducing SOC, each band splits into two singly degenerate bands, giving rise to more band crossings in the M_xy mirror plane. However, as noted earlier, only if the bands have opposite eigenvalues ($\pm i$) under mirror operation are the band crossings maintained. In KCu_2EuTe_4, the spinless DNL splits into two spinful WNLs as shown in red in the lower panel of Figure 5(d). The band projections of these states show that the WNLs are attributed to both the Eu and
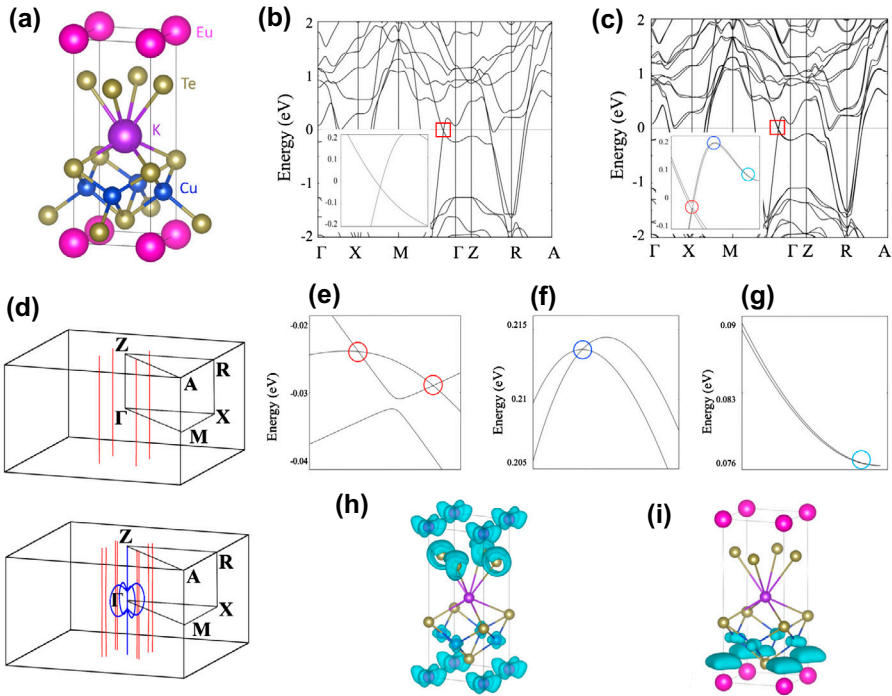
Figure 5. Crystal structure, band structure, and nodal line distribution of KCu_2EuTe_4. (a) Crystal structure of KCu_2EuTe_4. (b,c) Calculated bulk band structure of KCu_2EuTe_4 in paramagnetic phase without SOC and with SOC. (d) Nodal line distribution without (upper) and with SOC (lower). The red lines represent DNLs that are created and protected by mirror symmetry; the blue lines show the 'flower-shaped' WNLs that are generated by accidental band crossings upon considering SOC. (e–g) Zoom-in band structure along M–Γ with the inclusion of SOC. The crossings shown in (e) are responsible for the four Weyl nodal lines, in (f) corresponds to accidental 'flower-shaped' nodal rings, and in (g) is responsible for the accidental nodal line along C_4 axis. (h) Partial charge distribution of the states corresponding to the WNLs in (e). (i) Partial charge distribution of the states corresponding to the WNLs in (f) and (g).

Te sublattices, shown in Figure 5h. Similar to the inversion plus SOC-generated new crossing in $PbTaSe_2$, SOC in KCu_2EuTe_4 also generates a new accidental band crossing and a set of 'flower-shaped' Weyl nodal rings in the M_{xy} plane, appearing above the E_F shown in blue in the lower panel of Figure 5(d). Band projections show that mainly Eu sublattices contribute to these states (Figure 5(i)). A zoom-in view of the band between M and G with SOC are shown in Figures 5(e)–(g). Among them, the band structure shown in Figure 5(e) corresponds to the DNL split WNLs, Figure 5(f) corresponds to the crossing responsible for the 'flower shaped' nodal ring, and Figure 5(g) corresponds to inversion plus SOC newly generated nodal lines along the C_4 rotation axis.

It is also worth mentioning that aside from the nodal lines and rings discussed above, more crossings both above and below the E_F, within about 1 eV, are present, implying more interesting nodal lines/rings to be explored in this family

Table 8. Experimentally confirmed and theoretically predicted topological nodal line semimetals.

Materials	Symmetry	Topological type without SOC (+ SU(2))	Topological type with SOC	Gap size
$MSiS$ ($M = Zr$, Hf)	I + TR + mirror glide		DNLS	
AIrO$_3$	I + TR + mirror glide			
IrO$_2$	I + TR + mirror glide			
Pb(Tl)TaSe$_2$	Mirror		WNLS	
KCu$_2$EuTe$_4$	Mirror			
Cu$_3$NX ($X = $ Ni, Cu, Pd, An, Ag, Cd)	I + TR + C$_4$			
CaTe	I + TR + C$_4$		DSM	
LaX ($X = $ N, P, As, Sb, Bi)	I + TR + C$_4$			
TaAs	Mirror			
HfC	Mirror		WSM	
MTC	I + TR	DNLS		0.13 meV at 1.5 K
AX_2 ($A = $ Ca, Sr, Ba; $X = $ Si, Ge, Sn)	I + TR			< 160 meV
Hyperhoneycomb lattice	I + TR			N/A
Ca$_3$P family	I + TR		TI	From 1.76 meV to 47.14 meV
Ca$_3$P$_2$	I + TR + Mirror			9 meV
Cu$_2$Si	I + TR + Mirror			<15 meV
Hg$_3$As$_2$	I + TR + Mirror			34 meV
CaAgX ($X = $ P, As)	TR + Mirror			P = 1 meV; As = 75 meV

of compounds. Tuning the E_F and band structure via chemical control, similar to the ZrSiS family, should be possible. To the best of our knowledge, KCu_2EuTe_4 is the first predicted WNLS which have nodal lines almost exactly at the E_F, making it a good candidate to study the exotic physics related to WNLS. Transport and magnetic measurements by Kanatzidis et al indicate KCu_2EuTe_4 to be a paramagnetic metal or semimetal down to 2 K [155]. Their electron diffraction experiments revealed large amounts of twinning with possible superstructure peaks indicating a small structural distortion. However this has not been fully solved and is planned for future work. In addition, since some distorted square nets can be topologically equivalent to perfect square nets similar to how hyper-honeycomb lattices are topologically equivalent to perfect honeycombs, a rigorous study of the robustness of the various crossings to likely distortion modes is currently under preparation [101].

5. Summary and experimental outlook

Topological nodal line semimetals, as precursors of many other TSMs or TIs, have drawn great interest in the field of condensed matter physics in the last couple of years. The combination of inversion and time-reversal symmetry often generates nodal lines/rings; however, their protection against SOC requires one or more spatial symmetries, in particular, mirror reflection or non-symmorphic symmetry. Rotation symmetry can make DNLSs into DSMs or TIs. Mirror reflection symmetry can protect the degeneracy on the plane of the mirror, and non-symmorphic symmetry forces band degeneracies at high-symmetry points. Mirror reflections can generate new crossings rather than just split fourfold crossings when combined with a lack of inversion and large SOC. Table 5 summarizes the experimentally confirmed and theoretically predicted topological nodal line semimetals, their topological category without and with SOC, their gap size (if applicable) as well as their corresponding crystalline symmetries.

With several materials now predicted to house the exotic electronic structures of NLSs, future studies will focus on experimental investigation of the properties stemming from those electronic structures. Firstly, there is a large opportunity to characterize the NLSs using probes other than photoemisssion. As topological surface states is a characteristic signature of the non-trivial topology, direct probing of drumhead surface states is the next experimental step. The dispersion of the drumhead surface states is smaller than that of typical bulk valence and conduction bands, making them good candidates for studying correlation effects at surfaces [156]. It is proposed that in Dirac nodal ring systems, with coexistance of inversion and time-reversal symmetries as well as negligible SOC, and in the small Hubbard interaction region, surface ferromagnetism can be obtained and characterized by the surface mode divergence of the spin susceptibility [156]. Increasing the Hubbard interaction should drive the system into a surface

charge-ordered phase through a continuous quantum phase transition [156]. In addition, the bulk DNLs can also be investigated via transport measurements; Novel Landau level structures in nodal ring semimetals are predicted as a function of the strength and direction of applied magnetic fields [60,101]. Almost non-dispersive Landau levels, as a function of momentum, have been predicted when the magnetic field is applied in the plane of the ring. Near the center of the ring, almost flat Dirac zero modes are expected [60].

Aside from just the fundamental physics of topological nodal line semimetals, more applied investigations of these materials have also been proposed, for example, making future spintronic devices. One route to generating spin currents (necessary in spintronics) is to use the spin Hall effect (SHE), where electric current generates a transverse spin current. The intrinsic spin Hall conductivity (SHC) can be calculated by integrating the spin Berry curvature over the BZ. Since anti-crossings in the electronic structure induced by SOC can lead to a large Berry curvature, to maximize SHC, one needs to maximize the number of band anti-crossings (gapped by SOC) at E_F, among other parameters. A DNL consists of an infinite number of Dirac points along the line of degeneracy, and, unless protected by spatial symmetries as described earlier, is gapped due to SOC. Therefore, it is natural to think that gapped DNL materials have large intrinsic SHEs. It has recently been found the DNL in metallic rutile oxides IrO_2, OsO_2, and RuO_2 contribute to the large SHC in these materials [75].

The interaction of nodal line materials with light is another avenue for future work. It has been studied in DSMs and WSMs that circularly polarized light can couple with electrons and break the time-reversal symmetry of the material through the Floquet effect [62–64]. This light-induced interaction gives rise to a photovoltaic anomalous Hall effect as well as large photocurrents [157]. It has been theorized that such an interaction can also happen in NLSs, that circularly polarized light could break a nodal line into Weyl points accompanied by a signature of anomalous Hall conductivity tunable by the incident light [158–160]. The anomalous Hall conductivity depends largely on the location of E_F: when the degeneracy is at the E_F, the induced Hall conductivity depends on the radius of the nodal ring and not on intensity of the light. However, when the E_F is far away from the line node, the Hall conductivity does vary with the light intensity56. This dependence of Hall conductivity on E_F could have potential applications in phototransistors based on nodal line materials [158].

The recent advances in the theoretical understanding of NLS and specifically the underlying symmetry causes of DNLs and WNLs have led to the discovery of several good candidate materials. Now experimental investigation of the properties stemming from this novel physics is expected to develop and drive the next wave of topological physics studies, both in a fundamental as well as applied manner.

Author contributions

S.Y. Yang led the research effort and wrote the majority of the manuscript. H. Yang carried out the majority of the electronic structure calculations and identified the nodal lines of KCu_2EuTe_4. E. Derunova assisted in calculations and discussions. S.S.P Parkin, B. Yan, and M. N. Ali directed the research effort. All authors contributed to writing the manuscript. M. N. Ali is the principal investigator.

Acknowledgements

Disclosure statement

No potential conflict of interest was reported by the authors.

Funding

References

[1] M.Z. Hasan and C.L. Kane, Rev. Mod. Phys. 82 (2010) p.3045.
[2] X.-L. Qi and S.-C. Zhang, Rev. Mod. Phys 83 (2011) p.1057.
[3] N. Armitage, E. Mele and A. Vishwanath, preprint arXiv:1705.01111 (2017).
[4] Z. Wang, Y. Sun, X.-Q. Chen, C. Franchini, G. Xu, H. Weng, X. Dai and Z. Fang, Phys. Rev. B 85 (2012) p.195320.
[5] Z. Liu, B. Zhou, Y. Zhang, Z. Wang, H. Weng, D. Prabhakaran, S.-K. Mo, Z. Shen, Z. Fang, X. Dai, et al., Science 343 (2014) p.864.
[6] M. Neupane, S. Xu, R. Sankar, N. Alidoust, G. Bian, C. Liu, I. Belopolski, T. Chang, H. Jeng, H. Lin, et al., Nat. Commun. 5 (2014) p.3786.
[7] Z. Liu, J. Jiang, B. Zhou, Z. Wang, Y. Zhang, H. Weng, D. Prabhakaran, S. Mo, H. Peng, P. Dudin, et al., Nat. Mater. 13 (2014) p.677.
[8] S. Borisenko, Q. Gibson, D. Evtushinsky and V. Zabolotnyy, B. B ü chner, and R: J. Cava Phys. Rev. Lett. 113 (2014) p.027603.
[9] Z. Wang, H. Weng, Q. Wu, X. Dai and Z. Fang, Phys. Rev. B 88 (2013) p.125427.
[10] M.N. Ali, Q. Gibson, S. Jeon, B.B. Zhou, A. Yazdani and R. Cava, Inorg. Chem. 53 (2014) p.4062.
[11] S. Jeon, B.B. Zhou, A. Gyenis, B.E. Feldman, I. Kimchi, A.C. Potter, Q.D. Gibson, R.J. Cava, A. Vishwanath and A. Yazdani, Nat. Mater. 13 (2014) p.851.

[12] J. Feng, Y. Pang, D. Wu, Z. Wang, H. Weng, J. Li, X. Dai, Z. Fang, Y. Shi, and L. Lu Phys. Rev. B. 92 (2015), p. 081306.

[13] T. Liang, Q. Gibson, M.N. Ali, M. Liu, R. Cava and N. Ong, Nat. Mater. 14 (2015) p.280.

[14] L.X. Wang, C.-Z. Li, D.-P. Yu, and Z.-M. Liao Nat. Commun. 7 (2016) p.10769.

[15] H.B. Nielsen and M. Ninomiya, Nucl. Phys. B 185 (1981) p.20.

[16] H.B. Nielsen and M. Ninomiya, Nucl. Phys. B 193 (1981) p.173.

[17] Z. Fang, N. Nagaosa, K.S. Takahashi, A. Asamitsu, R. Mathieu, T. Ogasawara, H. Yamada, M. Kawasaki, Y. Tokura, and K. Terakura Science. 302 (2003), p. 92.

[18] X. Wan, A.M. Turner, A. Vishwanath and S.Y. Savrasov, Phys. Rev. B 83 (2011) p.205101.

[19] L. Balents, Physics 4 (2011) p.36.

[20] G. Xu, H. Weng, Z. Wang, X. Dai and Z. Fang, Phys. Rev. Lett. 107 (2011) p.186806.

[21] H. Weng, C. Fang, Z. Fang, B.A. Bernevig and X. Dai, Phys. Rev. X 5 (2015) p.011029.

[22] S.-M. Huang, S.-Y. Xu, I. Belopolski, C.-C. Lee, G. Chang, B. Wang, N. Alidoust, G. Bian, M. Neupane, C. Zhang and S. Jia, Nat. Commun. 6 (2015) p.7373.

[23] H.B. Nielsen and M. Ninomiya, Phys. Lett. B 130 (1983) p.389.

[24] P. Hosur, S. Parameswaran and A. Vishwanath, Phys. Rev. Lett. 108 (2012) p.046602.

[25] D. Son and B. Spivak, Phys. Rev. B 88 (2013) p.104412.

[26] H.-J. Kim, K.-S. Kim, J.-F. Wang, M. Sasaki, N. Satoh, A. Ohnishi, M. Kitaura, M. Yang, and L. Li Phys. Rev. Lett. 111 (2013), p. 246603.

[27] S. Parameswaran, T. Grover, D. Abanin, D. Pesin and A. Vishwanath, Phys. Rev. X 4 (2014) p.031035.

[28] J. Xiong, S.K. Kushwaha, T. Liang, J.W. Krizan, M. Hirschberger, W. Wang, R. Cava and N. Ong, Science 350 (2015) p.413.

[29] C.-Z. Li, L.-X. Wang, H. Liu, J. Wang, Z.-M. Liao and D.-P. Yu, Nat. Commun. 6 (2015), p. 10137.

[30] F. Arnold, C. Shekhar, S.-C. Wu, Y. Sun, R.D. Dos Reis, N. Kumar, M. Naumann, M.O. Ajeesh, M. Schmidt, A.G. Grushin and J.H. Bardarson, Nat. Commun. 7 (2016), p. 11615.

[31] C. Zhang, E. Zhang, W. Wang, Y. Liu, Z.-G. Chen, S. Lu, S. Liang, J. Cao, X. Yuan, L. Tang and Q. Li, Nat. Commun. 8 (2017) p.13741.

[32] M. Hirschberger, S. Kushwaha, Z. Wang, Q. Gibson, S. Liang, C. Belvin, B. Bernevig, R. Cava and N. Ong, Nat. Mater. 15 (2016), p. 1161.

[33] P. Hosur and X. Qi, C.R. Phys. 14 (2013), p. 857.

[34] G. Volovik, Physica Scripta 2015 (2015) p.014014.

[35] S.-Y. Xu, I. Belopolski, N. Alidoust, M. Neupane, G. Bian, C. Zhang, R. Sankar, G. Chang, Z. Yuan, C.-C. Lee and S.-M. Huang, Science. 349 (2015), p. 613.

[36] B. Lv, H. Weng, B. Fu, X. Wang, H. Miao, J. Ma, P. Richard, X. Huang, L. Zhao, G. Chen and Z. Fang, Phys. Rev. X 5 (2015) p.031013.

[37] L. Yang, Z. Liu, Y. Sun, H. Peng, H. Yang, T. Zhang, B. Zhou, Y. Zhang, Y. Guo, M. Rahn and D. Prabhakaran, Nat. Phys. 11 (2015) p.728.

[38] S.-Y. Xu, N. Alidoust, I. Belopolski, Z. Yuan, G. Bian, T.-R. Chang, H. Zheng, V.N. Strocov, D.S. Sanchez, G. Chang and C. Zhang, Nat. Phys. 11 (2015), p. 748.

[39] S. Souma, Z. Wang, H. Kotaka, T. Sato, K. Nakayama, Y. Tanaka, H. Kimizuka, T. Takahashi, K. Yamauchi, T. Oguchi and K. Segawa, Phys. Rev. B 93 (2016) p.161112.

[40] Z. Liu, L. Yang, Y. Sun, T. Zhang, H. Peng, H. Yang, C. Chen, Y. Zhang, Y. Guo, D. Prabhakaran and M. Schmidt, Nat. Mater. 15 (2016) p.27.

[41] L. Lu, Z. Wang, D. Ye, L. Ran, L. Fu and J.D. Joannopoulos, and M: Solja č i ć, Science 349 (2015) p.622.

[42] A.A. Soluyanov, D. Gresch, Z. Wang, Q. Wu, M. Troyer, X. Dai and B.A. Bernevig, Nature 527 (2015) p.495.

[43] Y. Sun, S.-C. Wu, M.N. Ali, C. Felser and B. Yan, Phys. Rev. B 92 (2015) p.161107.

[44] L. Huang, T.M. McCormick, M. Ochi, Z. Zhao, M.-T. Suzuki, R. Arita, Y. Wu, D. Mou, H. Cao, J. Yan and N. Trivedi, Nat. Mater. 15 (2016) p.1155.

[45] K. Deng, G. Wan, P. Deng, K. Zhang, S. Ding, E. Wang, M. Yan, H. Huang, H. Zhang, Z. Xu and J. Denlinger, Nat. Phys. 12 (2016) p.1105.

[46] J. Jiang, Z. Liu, Y. Sun, H. Yang, C. Rajamathi, Y. Qi, L. Yang, C. Chen, H. Peng, C. Hwang and S.-Z. Sun, Nat. Commun. 8 (2017) p.13973.

[47] A. Tamai, Q. Wu, F.Y. Bruno, I. Cucchi, S. Riccò, T. Kim, M. Hoesch, C. Barreteau, E. Giannini, C. Besnard and A.-A. Soluyanov, Phys. Rev. X. 6 (2016), p. 031021.

[48] X. Huang, L. Zhao, Y. Long, P. Wang, D. Chen, Z. Yang, H. Liang, M. Xue, H. Weng, Z. Fang and X. Dai, Phys. Rev. X 5 (2015) p.031023.

[49] J. Du, H. Wang, Q. Chen, Q. Mao, R. Khan, B. Xu, Y. Zhou, Y. Zhang, J. Yang, B. Chen and C. Fang, Sci. China Phys. Mech. Astron. 59 (2016) p.1.

[50] X. Yang, Y. Liu, Z. Wang, Y. Zheng and Z.-A. Xu, preprint arXiv:1506.03190 (2015).

[51] M. Ali, J. Xiong, S. Flynn, J. Tao, Q. Gibson, L. Schoop, T. Liang, N. Haldolaarachchige, M. Hirschberger, N. Ong and R. Cava, Nature. 514 (2014), p. 205.

[52] C. Shekhar, A.K. Nayak, Y. Sun, M. Schmidt, M. Nicklas, I. Leermakers, U. Zeitler, Y. Skourski, J. Wosnitza, Z. Liu and Y. Chen, Nat. Phys. 11 (2015) p.645.

[53] T. Bzdusek, Q. Wu, A. Ruegg, M. Sigrist and A. Soluyanov, Nature 538 (2016) p.75.

[54] H. Weng, Y. Liang, Q. Xu, R. Yu, Z. Fang, X. Dai and Y. Kawazoe, Phys. Rev. B 92 (2015) p.045108.

[55] A. Burkov, M. Hook and L. Balents, Phys. Rev. B 84 (2011) p.235126.

[56] T.T. Heikkilä and G.E. Volovik, JETP Lett. 93 (2011), p. 59.

[57] N. Kopnin, T. Heikkil ä and G. Volovik, Phys. Rev. B 83 (2011) p.220503.

[58] T.T. Heikkilä, N.B. Kopnin, and G.E. Volovik, JETP Lett. 94 (2011), p. 233.

[59] Y. Huh, E.-G. Moon and Y.B. Kim, Phys. Rev. B 93 (2016) p.035138.

[60] J.-W. Rhim and Y.B. Kim, Phys. Rev. B 92 (2015) p.045126.

[61] S.T. Ramamurthy and T.L. Hughes, preprint arXiv:1508.01205 (2015).

[62] S. Ebihara, K. Fukushima and T. Oka, Phys. Rev. B 93 (2016) p.155107.

[63] C.-K. Chan, P.A. Lee, K.S. Burch, J.H. Han and Y. Ran, Phys. Rev. Lett. 116 (2016) p.026805.

[64] K. Taguchi, T. Imaeda, M. Sato and Y. Tanaka, Phys. Rev. B 93 (2016) p.201202.

[65] R. Takahashi, M. Hirayama and S. Murakami, preprint arXiv:1704.02151 (2017).

[66] C. Fang, Y. Chen, H.-Y. Kee and L. Fu, Phys. Rev. B 92 (2015) p.081201.

[67] C. Fang, H. Weng, X. Dai and Z. Fang, Chin. Phys. B 25 (2016) p.117106.

[68] B. Yan, and C. Felser, Annu. Rev. Condens. Matter Phys. 8 (2017), p. 337.

[69] S. Jia, S.-Y. Xu and M.Z. Hasan, Nat. Mater. 15 (2016) p.1140.

[70] S. Wang, B.-C. Lin, A.-Q. Wang, D.-P. Yu and Z.-M. Liao Adv. Phys.: X. 2 (2017), p. 518.

[71] R. Yu, Z. Fang, X. Dai and H. Weng, Front. Phys. 12 (2017) p.127202.

[72] H. Weng, X. Dai and Z. Fang, J. Phys.: Condens. Matter 28 (2016) p.303001.

[73] G. Bian, T.-R. Chang, R. Sankar, S.-Y. Xu, H. Zheng, T. Neupert, C.-K. Chiu, S.-M. Huang, G. Chang, I. Belopolski and D.-S. Sanchez, Nat. Commun. 7 (2016) p.10556.

[74] L.M. Schoop, M.N. Ali, C. Straßer, A. Topp, A. Varykhalov, D. Marchenko, V. Duppel, S.S. Parkin, B.V. Lotsch and C.R. Ast Nat. Commun. 7 (2016), p. 11696.

[75] Y. Sun, Y. Zhang, C.-X. Liu, C. Felser and B. Yan, preprint arXiv:1701.09089 (2017).

[76] Z. Liu, M. Li, Q. Li, J. Liu, W. Li, H. Yang, Q. Yao, C. Fan, X. Wan, Z. Wang and D.-W. Shen, Sci. Rep. 6 (2016) p.30309.

[77] M. Neupane, I. Belopolski, M.M. Hosen, D.S. Sanchez, R. Sankar, M. Szlawska, S.-Y. Xu, K. Dimitri, N. Dhakal, P. Maldonado and P.-M. Oppeneer, Phys. Rev. B 93 (2016) p.201104.

[78] C. Chen, X. Xu, J. Jiang, S.-C. Wu, Y. Qi, L. Yang, M. Wang, Y. Sun, N. Schröter, H. Yang, et al, Phys. Rev. B 95 (2017) p.125126.

[79] M.N. Ali, Q.D. Gibson, T. Klimczuk and R. Cava, Phys. Rev. B 89 (2014) p.020505.

[80] S.-Y. Guan, P.-J. Chen, M.-W. Chu, R. Sankar, F. Chou, H.-T. Jeng, C.-S. Chang and T.-M. Chaung Sci. Adv. 2 (2016), p. e1600894.

[81] T.-R. Chang, P.-J. Chen, G. Bian, S.-M. Huang, H. Zheng, T. Neupert, R. Sankar, S.-Y. Xu, I. Belopolski, G. Chang and B. Wang, Phys. Rev. B 93 (2016) p.245130.

[82] G. Bian, T.-R. Chang, H. Zheng, S. Velury, S.-Y. Xu, T. Neupert, C.-K. Chiu, S.-M. Huang, D.S. Sanchez, I. Belopolski and N. Alidoust, Phys. Rev. B 93 (2016) p.121113.

[83] Y. Kim, B.J. Wieder, C. Kane and A.M. Rappe, Phys. Rev. Lett. 115 (2015) p.036806.

[84] R. Yu, H. Weng, Z. Fang, X. Dai and X. Hu, Phys. Rev. Lett. 115 (2015) p.036807.

[85] R. Yu, Q. Wu, Z. Fang and H. Weng, Phys. Rev. Lett. 119 (2017) p.036401.

[86] Q. Gibson, L. Schoop, L. Muechler, L. Xie, M. Hirschberger, N. Ong, R. Car and R. Cava, Phys. Rev. B. 91 p. 205128.

[87] S.M. Young and C.L. Kane, Phys. Rev. Lett. 115 (2015) p.126803.

[88] S. Murakami, *Topological Matter – Topological Insulators, Skyrmions and Majoranas*, Lecture notes, 2017, p.B2.13.

[89] Y.-H. Chan, C.-K. Chiu, M. Chou and A.P. Schnyder, Phys. Rev. B 93 (2016) p.205132.

[90] R. Hoffmann, Angew. Chem. Int. Ed. English. 26 (1987), p. 846.

[91] W. Tremel and R. Hoffmann, J. Am. Chem. Soc 109 (1987) p.124.

[92] Y. Du, F. Tang, D. Wang, L. Sheng, E.-J. Kan, C.-G. Duan, S.Y. Savrasov and X. Wan, npj Quant. Mater. 2 (2017) p.3.

[93] M. Zeng, C. Fang, G. Chang, Y.-A. Chen, T. Hsieh, A. Bansil, H. Lin and L. Fu, preprint arXiv:1504.03492 (2015).

[94] L.S. Xie, L.M. Schoop, E.M. Seibel, Q.D. Gibson, W. Xie and R.J. Cava, APL Mater. 3 (2015) p.083602.

[95] Q. Xu, R. Yu, Z. Fang, X. Dai and H. Weng, Phys. Rev. B 95 (2017) p.045136.

[96] H. Huang, J. Liu, D. Vanderbilt and W. Duan, Phys. Rev. B 93 (2016) p.201114.

[97] J. Nayak, S.-C. Wu, N. Kumar, C. Shekhar, S. Singh, J. Fink, E.E. Rienks, G.H. Fecher, S.S. Parkin, B. Yan, et al. Nat. Commun. 8 (2017).

[98] X. Feng,, C. Yue, Z. Song, Q. Wu and B. Wen, preprint arXiv:1705.00511 (2017).

[99] R. Kumar, M. Mishra, B. Sharma, V. Sharma, J. Lowther, V. Vyas and G. Sharma, Comput. Mater. Sci. 61 (2012) p.150.

[100] X. Zhang, Z.-M. Yu, X.-L. Sheng, H.Y. Yang and S.A. Yang, Phys. Rev. B 95 (2017) p.235116.

[101] K. Mullen, B. Uchoa and D.T. Glatzhofer, Phys. Rev. Lett. 115 (2015) p.026403.

[102] B. Feng, B. Fu, S. Kasamatsu, S. Ito, P. Cheng, C.-C. Liu, S.K. Mahatha, P. Sheverdyaeva, P. Moras, M. Arita and O. Sugino, preprint arXiv:1611.09578 (2016).

[103] J. Lu, W. Luo, X. Li, S. Yang, J. Cao, X. Gong and H. Xiang, preprint arXiv:1603.04596 (2016).

[104] F.F. Tafti, Q. Gibson, S. Kushwaha, J.W. Krizan, N. Haldolaarachchige and R.J. Cava, Proc. Nat. Acad. Sci. 113 (2016) p.E3475.

[105] F. Tafti, Q. Gibson, S. Kushwaha, N. Haldolaarachchige and R. Cava, Nat. Phys. 12 (2016) p.272.

[106] N. Kumar, C. Shekhar, S.-C. Wu, I. Leermakers, O. Young, U. Zeitler, B. Yan and C. Felser, Phys. Rev. B. 93 (2016), p. 241106.

[107] L.-K. Zeng, R. Lou, D.-S. Wu, Q. Xu, P.-J. Guo, L.-Y. Kong, Y.-G. Zhong, J.-Z. Ma, B.-B. Fu, P. Richard and P. Wang, Phys. Rev. Lett. 117 (2016) p.127204.

[108] Y. Wu, T. Kong, L.-L. Wang, D.D. Johnson, D. Mou, L. Huang, B. Schrunk, S.L. Bud'ko, P.C. Canfield and A. Kaminski, Phys. Rev. B. 94 (2016), p. 081108.

[109] A. Wa ś kowska, L. Gerward, J.S. Olsen, K.R. Babu, G. Vaitheeswaran, V. Kanchana, A. Svane, V. Filipov, G. Levchenko and A. Lyaschenko, Acta Mater. 59 (2011), p. 4886.

[110] N.L. Okamoto, M. Kusakari, K. Tanaka, H. Inui and S. Otani, Acta Mater. 58 (2010) p.76.

[111] M. Ezawa, Phys. Rev. Lett. 116 (2016), p. 127202.

[112] E.K.-H. Lee, S. Bhattacharjee, K. Hwang, H.-S. Kim, H. Jin and Y.B. Kim, Phys. Rev. B 89 (2014) p.205132.

[113] T. Takayama, A. Kato, R. Dinnebier, J. Nuss, H. Kono, L. Veiga, G. Fabbris, D. Haskel and H. Takagi, Phys. Rev. Lett. 114 (2015), p. 077202.

[114] A. Biffin, R. Johnson, S. Choi, F. Freund, S. Manni, A. Bombardi, P. Manuel, P. Gegenwart and R. Coldea, Phys. Rev. B. 90 (2014), p. 205116.

[115] K. A, T. E, I. Kimchi, N.P. Breznay, A. Biffin, S. Choi, R.D. Johnson, R. Coldea, P. Watkins-Curry, G.T. McCandless and J.-Y. Chan, preprint arXiv:1402.3254 (2014).

[116] E.K.H. Lee, R. Schaffer, S. Bhattacharjee and Y.B. Kim, Phys. Rev. B. 89 (2014), p. 045117.

[117] I. Kimchi and J.G. Analytis, and A: Vishwanath Phys. Rev. B 90 (2014) p.205126.

[118] S. Lee, E.K.-H. Lee, A. Paramekanti and Y.B. Kim, Phys. Rev. B 89 (2014) p.014424.

[119] G. Pang, M. Smidman, L. Zhao, Y. Wang, Z. Weng, L. Che, Y. Chen, X. Lu, G. Chen and H. Yuan, Phys. Rev. B 93 (2016) p.060506.

[120] L. Zhang, Z. Yuan, G. Bian, S.-Y. Xu, X. Zhang, M.Z. Hasan and S. Jia, Phys. Rev. B. 93 (2016), p. 054520.

[121] R. Sankar, G.N. Rao, I.P. Muthuselvam, T.-R. Chang, H. Jeng, G.S. Murugan, W.-L. Lee and F. Chou, J. Phys.: Condens. Matter 29 (2017) p.095601.

[122] I. Belopolski, S.-Y. Xu, D.S. Sanchez, G. Chang, C. Guo, M. Neupane, H. Zheng, C.-C. Lee, S.-M. Huang, G. Bian and N. Alidoust, Phys. Rev. Lett. 116 (2016), p. 066802.

[123] H. Inoue, A. Gyenis, Z. Wang, J. Li, S.W. Oh, S. Jiang, N. Ni, B.A. Bernevig and A. Yazdani, Science 351 (2016) p.1184.

[124] R. Batabyal, N. Morali, N. Avraham, Y. Sun, M. Schmidt, C. Felser, A. Stern, B. Yan and H. Beidenkopf, Sci. Adv. 2 (2016), p. e1600709.

[125] N.J. Ghimire, Y. Luo, M. Neupane, D. Williams, E. Bauer and F. Ronning, J. Phys.: Condens. Matter 27 (2015) p.152201.

[126] Z. Wang, Y. Zheng, Z. Shen, Y. Lu, H. Fang, F. Sheng, Y. Zhou, X. Yang, Y. Li, C. Feng and Z.-A. Xu, Phys. Rev. B 93 (2016) p.121112.

[127] C.-L. Zhang, S.-Y. Xu, I. Belopolski, Z. Yuan, Z. Lin, B. Tong, G. Bian, N. Alidoust, C.-C. Lee, S.-M. Huang and T.-R. Chang, Nat. Commun. 7 (2016).

[128] Y. Luo, N. Ghimire, M. Wartenbe, H. Choi, M. Neupane, R. McDonald, E. Bauer, J. Zhu and J. Thompson, and F: Ronning Phys. Rev. B 92 (2015) p.205134.

[129] P.J. Moll, A.C. Potter, N.L. Nair, B. Ramshav, K. Modic, S. Riggs, B. Zheng, N.J. Ghimire, E.D. Bauer, R. Kealhofer and F. Ronning, Nat. Commun. 7 (2016).

[130] A. Yamakage, Y. Yamakawa, Y. Tanaka and Y. Okamoto, J. Phys. Soc. Jpn 85 (2015) p.013708.

[131] D. Takane, Z. Wang, S. Souma, K. Nakayama, C. Trang, T. Sato, T. Takahashi and Y. Ando, Phys. Rev. B 94 (2016) p.121108.

[132] M.N. Ali, L.M. Schoop, C. Garg, J.M. Lippmann, E. Lara, B. Lotsch and S. Parkin, preprint arXiv:1603.09318 (2016).

[133] X. Wang, X. Pan, M. Gao, J. Yu, J. Jiang, J. Zhang, H. Zuo, M. Zhang, Z. Wei, W. Niu, et al., preprint arXiv:1604.00108 (2016).

[134] R. Singha, A. Pariari, B. Satpati, and P. Mandal, preprint arXiv:1602.01993 (2016).

[135] J. Hu, Z. Tang, J. Liu, Y. Zhu, J. Wei and Z. Mao, preprint arXiv:1604.01567 (2016).

[136] N. Kumar, K. Manna, Y. Qi, Y. Qi, S.-C. Wu, L. Wang, B. Yan, C. Felser and C. Shekhar, preprint arXiv:1612.05176 (2016).

[137] A. Topp, J.M. Lippmann, A. Varykhalov, V. Duppel, B.V. Lotsch, C.R. Ast and L.M. Schoop, New J. Phys. 18 (2016) p.125014.

[138] Y.-Y. Lv, B.-B. Zhang, X. Li, S.-H. Yao, Y. Chen, J. Zhou, S.-T. Zhang, M.-H. Lu and Y.-F. Chen, Appl. Phys. Lett. 108 (2016) p.244101.

[139] Y. Nie, P. King, C. Kim, M. Uchida, H. Wei, B. Faeth, J. Ruf, J. Ruff, L. Xie, X. Pan and C.J. Fennie, Phys. Rev. Lett. 114 (2015) p.016401.

[140] J.K. Kawasaki, M. Uchida, H. Paik, D.G. Schlom and K.M. Shen, Phys. Rev. B 94 (2016) p.121104.

[141] R. Lou, J.-Z. Ma, Q.-N. Xu, B.-B. Fu, L.-Y. Kong, Y.-G. Shi, P. Richard, H.-M. Weng, Z. Fang, S.-S. Sun and Q. Wang, Phys. Rev. B 93 (2016) p.241104.

[142] J. Hu, Z. Tang, J. Liu, X. Liu, Y. Zhu, D. Graf, K. Myhro, S. Tran, C.N. Lau, J. Wei and Z. Mao, Phys. Rev. Lett. 117 (2016) p.016602.

[143] Q. Xu, Z. Song, S. Nie, H. Weng, Z. Fang and X. Dai, Phys. Rev. B. 92 (2015), p. 205310.

[144] Y. Chen, Y.-M. Lu and H.-Y. Kee, Nat. Commun. 6 (2015) p.6593.

[145] M.A. Zeb and H.Y. Kee, Phys. Rev. B. 86 (2012), p. 085149.

[146] J.-M. Carter, V.V. Shankar, M.A. Zeb and H.-Y. Kee, Phys. Rev. B 85 (2012) p.115105.

[147] J. Liu, D. Kriegner, L. Horak, D. Puggioni, C.R. Serrao, R. Chen, D. Yi, C. Frontera, V. Holy, A. Vishwanath and J.M. Rondinelli, Phys. Rev. B 93 (2016) p.085118.

[148] J. Fujioka, T. Okawa, A. Yamamoto and Y. Tokura, Phys. Rev. B 95 (2017) p.121102.

[149] L. Zhang, Y. Chen, B. Zhang, J. Zhou, S. Zhang, Z. Gu, S. Yao and Y. Chen, J. Phys. Soc. Japan 83 (2014) p.054707.

[150] J.H. Gruenewald, J. Nichols, J. Terzic, G. Cao, J.W. Brill and S.S.A. Seo, J. Mater. Res. 29 (2014) p.2491.

[151] A. Biswas, K.-S. Kim and Y.H. Jeong, J. Appl. Phys. 116 (2014) p.213704.

[152] A.P. Schnyder, S. Ryu, A. Furusaki and A.W. Ludwig, Phys. Rev. B 78 (2008) p.195125.

[153] J. Lin, S. Huang, Y. Lin, T. Lee, H. Liu, X. Zhang, R. Chen and Y. Huang, J. Phys.: Condens. Matter 16 (2004) p.8035.

[154] W. Ryden, W. Reed and E. Greiner, Phys. Rev. B 6 (1972) p.2089.

[155] R. Patschke, P. Brazis, C.R. Kannewurf and M.G. Kanatzidis, J. Mater. Chem. 9 (1999) p.2293.

[156] J. Liu and L. Balents, Phys. Rev. B 95 (2017) p.075426.

[157] C.-K. Chan, N.H. Lindner, G. Refael and P.A. Lee, Phys. Rev. B 95 (2017) p.041104.

[158] K. Taguchi, D.-H. Xu, A. Yamakage and K. Law, Phys. Rev. B 94 (2016) p.155206.

[159] Z. Yan and Z. Wang, Phys. Rev. Lett. 117 (2016) p.087402.

[160] M. Ezawa, preprint arXiv:1705.02140 (2017).